Electronic Supplementary Material (ESI) for Journal of Materials Chemistry C.

Supporting information

Precisely controllable fabrication of Er^{3+}-doped glass ceramic fibers: A novel mid-infrared fiber laser materials

Shiliang Kang[a], Zaijin Fang[a, b], Xiongjian Huang[a], Zhi Chen[a], Dandan Yang[a], Xiudi Xiao[c], Jianrong Qiu[d], Guoping Dong[a, †]

[a]State Key Laboratory of Luminescent Materials and Devices and Guangdong Provincial Key Laboratory of Fiber Laser Materials and Applied Techniques, School of Materials Science and Engineering, South China University of Technology, Guangzhou 510640, China

[b]Key Lab of In-fiber Integrated Optics, Ministry Education of China, Harbin Engineering University, Harbin, 150001, China

[c]Key Laboratory of Renewable Energy, Guangdong Key Laboratory of New and Renewable Energy Research and Development, Guangzhou Institute of Energy Conversion, Chinese Academy of Sciences, Guangzhou 510640, China

[d]College of Optical Science and Engineering, State Key Laboratory of Modern Optical Instrumentation, Zhejiang University, Hangzhou 310027, China

[†]Correspondence to [dgp@scut.edu.cn (G. Dong)]

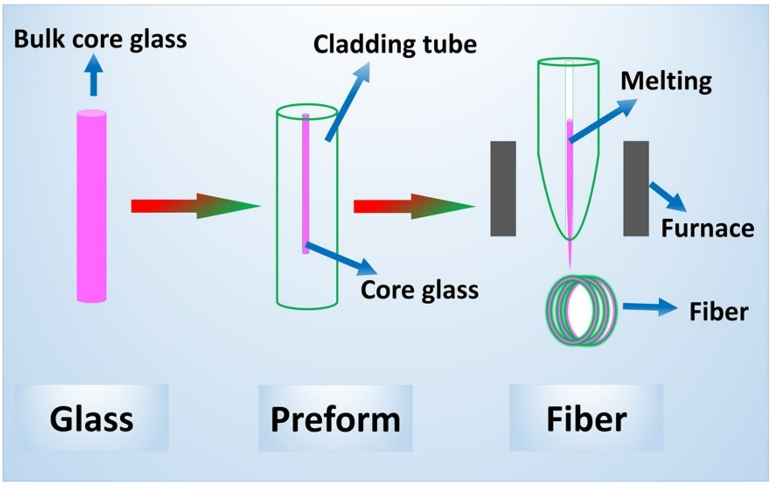

Figure S1. Schematic diagram of melt-in-tube technique. The bulk core glass is firstly prepared by the conventional melt-quenching method. Then the core glass is grinded and drilled to produce a cylindrical rod. The rod is polished, etched by acid and inserted into a cladding glass tube to form a preform. The key of melt-in-tube technique is that the cladding glass using high melting-point glass while the core glass using low melting-point glass. Therefore, during the fiber-drawing process, the core glass is melted while the cladding glass is softened. Since the core glass can be cooled down quickly to room temperature, the obtained fibers maintain amorphous state after the drawing process.

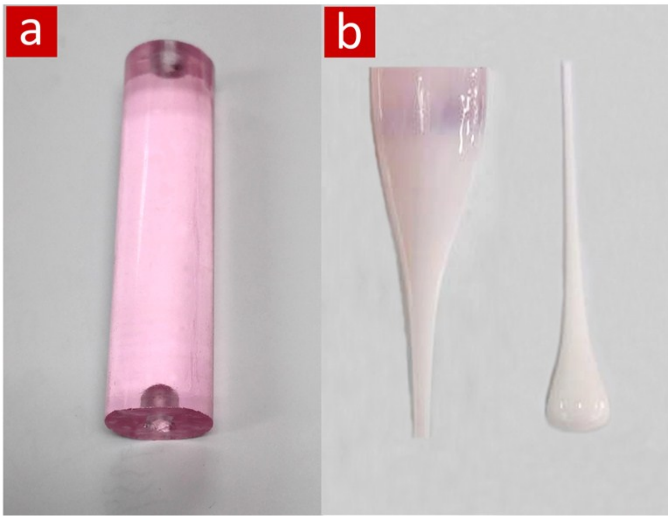

Figure S2. Images of core glass before a) and after b) drawn by traditional rod-in-tube technique. The precursor glass rod is transparent before the fiber-drawing process. However, it becomes completely opaque after drawn by traditional rod-in-tube technique at a temperature of 670 °C, which results in high transmission loss and fluorescence quenching. Therefore, the traditional rod-in-tube technique is not suitable for the fabrication of GC fibers.

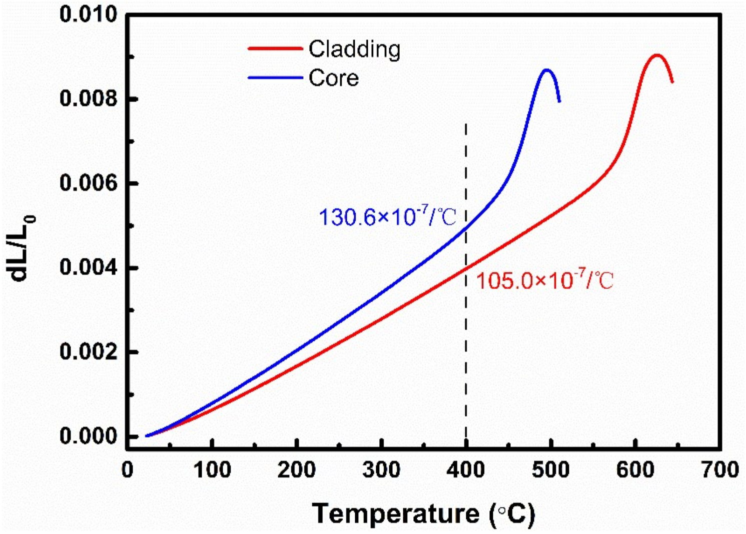

Figure S3. The thermal expansion coefficient of fiber core and cladding glasses. The thermal expansion coefficient of fiber core and cladding glasses at 400 °C are 130.6×10^{-7}/°C and 105.0×10^{-7}/°C, respectively. The small thermal expansion coefficient difference between fiber core and cladding can prevent fiber core from fracture during the cooling process.

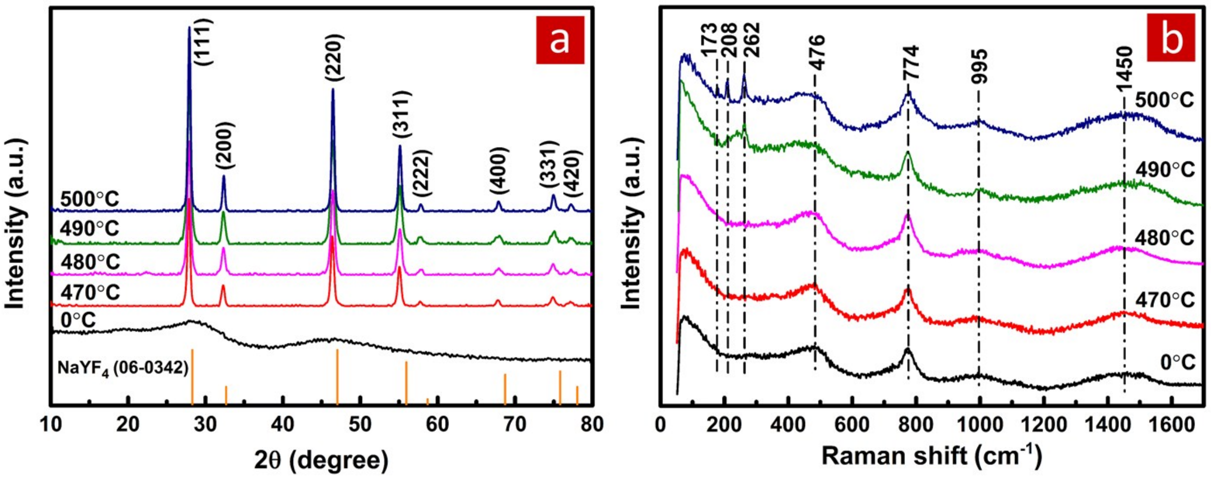

Figure S4. a) XRD patterns, and b) Raman spectra of precursor glass and GCs heat-treated at 470 ^{o}C-500 ^{o}C for 5 h. The precursor glass is completely amorphous with no diffraction peaks. After a heat-treatment process, strong diffraction peaks appear, which are easily assigned to the cubic $NaYF_4$ nanocrystal (JCPDS: 06-0342). With increasing crystallization temperature, the diffraction peaks become more obvious and sharper, which indicates that crystalline size increases. The Raman spectra of precursor glass is similar to those of borosilicate glasses, consisting of several bands at 476 cm^{-1}, 774 cm^{-1}, 995 cm^{-1}, and 1450 cm^{-1}.[1] By increasing the heat-treatment temperature, the sharp peaks located at 173 cm^{-1}, 208 cm^{-1} and 262 cm^{-1} are observed in the spectra, corresponding to the characteristic Raman bands of cubic $NaYF_4$ crystal,[2] which indicates that $NaYF_4$ nanocrystal have been formed in glass matrix.

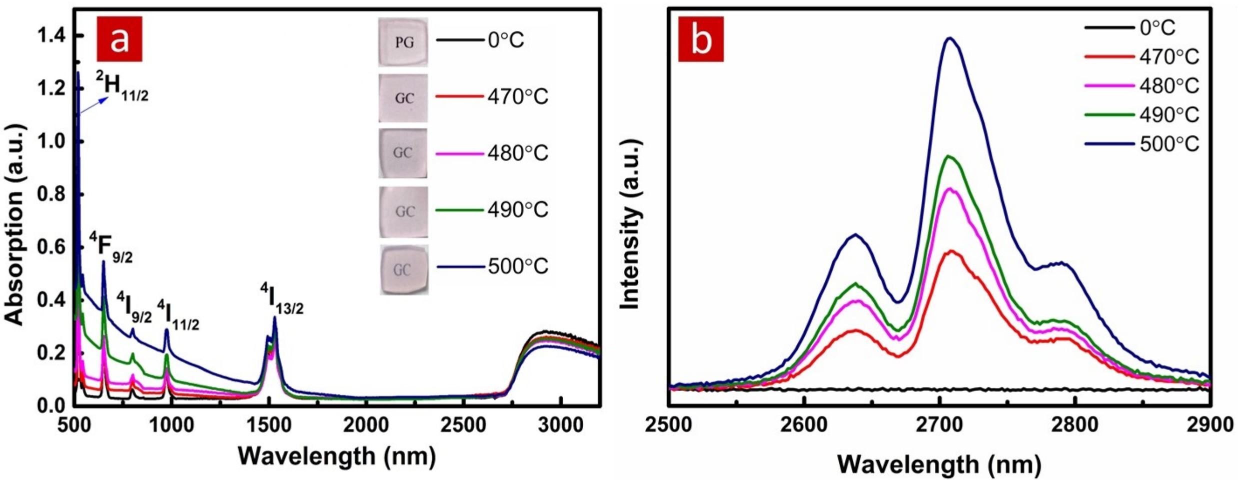

Figure S5. a) Absorption spectra, and b) 2.7 μm emission spectra of precursor glass and GCs heat-treated at 470 °C-500 °C for 5 h. The inset of Figure (a) shows the images of precursor glass and GCs. It can be seen that five absorption bands are centered at 1530 nm, 976 nm, 800 nm, 652 nm, 521 nm, corresponding to the transitions from ground state $^4I_{15/2}$ to excited levels $^4I_{13/2}$, $^4I_{11/2}$, $^4I_{9/2}$, $^4F_{9/2}$, and $^2H_{11/2}$ of Er^{3+} ions. With increasing heat-treatment temperature, the baselines of the absorption curves become more and more precipitous toward to the shorter wavelength region. It can be attributed to the transmittance loss caused by the Rayleigh scatting effect, which is resulted from the growth of $NaYF_4$ nanocrystals. The GCs still retain transparency after the heat-treatment process. Upon excitation with a 980 nm LD, the 2.7 μm emission of Er^{3+} can hardly be detected in the precursor glass. However, with the increase of heat-treatment temperature, enhanced 2.7 μm emission can be observed in the GCs, which is owing to the incorporation of Er^{3+} ions into the low phonon energy $NaYF_4$ nanocrystals.

Table S1. The J-O parameters of Er^{3+} in various samples

Samples	Ω_2 ($\times 10^{-20}$ cm^2)	Ω_4 ($\times 10^{-20}$ cm^2)	Ω_6 ($\times 10^{-20}$ cm^2)	δ ($\times 10^{-6}$)
precursor	3.96±0.05	1.24±0.07	0.69±0.05	0.13
470 °C	3.79±0.03	1.21±0.05	0.74±0.03	0.12
480 °C	3.70±0.04	1.22±0.03	0.75±0.10	0.14
490 °C	3.63±0.05	1.18±0.09	0.78±0.05	0.17
500 °C	3.57±0.05	1.19±0.11	0.80±0.03	0.13

On the basis of the absorption spectra, the J-O intensity parameters Ω_λ ($\lambda = 2, 4, 6$) of Er^{3+} in various samples have been determined. According to the J-O theory,[3] Ω_2 correlates with the asymmetry of the local environment around the site of Er^{3+}, and it decreases with the host changing from oxides to fluorides. It can be obtained from Table S1 that the Ω_2 decreases with increasing heat-treatment temperature, suggesting Er^{3+} ions are successfully incorporated into $NaYF_4$ nanocrystals. The root mean square deviation is less than 0.17×10^{-6}, indicating that the calculation process is valid and reliable.

Table S2. The spontaneous radiative transition probabilities, branching ratios and radiative lifetimes of Er^{3+} in various samples

Transitions	0 ^{o}C			470 ^{o}C			480 ^{o}C		
	$A_{rad}(s^{-1})$	β	τ_{rad}(ms)	$A_{rad}(s^{-1})$	β	τ_{rad}(ms)	$A_{rad}(s^{-1})$	β	τ_{rad}(ms)
$^4I_{13/2}\rightarrow{}^4I_{15/2}$	114.53	1	8.73	116.93	1	8.55	119.64	1	8.36
$^4I_{11/2}\rightarrow{}^4I_{15/2}$	104.67	0.83	7.93	104.90	0.82	7.82	106.18	0.81	7.63
$\rightarrow{}^4I_{13/2}$	22.06	0.17		23.79	0.18		25.23	0.19	
$^4I_{9/2}\rightarrow{}^4I_{15/2}$	99.87	0.79	7.91	99.82	0.78	7.81	101.32	0.77	7.60
$\rightarrow{}^4I_{13/2}$	26.10	0.21		28.53	0.22		31.05	0.23	
$^4F_{9/2}\rightarrow{}^4I_{15/2}$	1006.43	0.91	0.90	1034.76	0.91	0.88	1050.2	0.91	0.87
$\rightarrow{}^4I_{13/2}$	54.79	0.05		55.61	0.05		56.18	0.05	
$\rightarrow{}^4I_{11/2}$	41.45	0.04		44.25	0.04		44.71	0.04	
$\rightarrow{}^4I_{9/2}$	2.52	0		2.47	0		2.43	0	
$^4S_{3/2}\rightarrow{}^4I_{15/2}$	696.2	0.67	0.96	741.06	0.67	0.90	754.72	0.67	0.89
$\rightarrow{}^4I_{13/2}$	278.22	0.27		304.91	0.27		310.53	0.27	
$\rightarrow{}^4I_{11/2}$	22.33	0.02		24.30	0.02		24.74	0.02	
$\rightarrow{}^4I_{9/2}$	38.86	0.04		41.29	0.04		41.98	0.04	

Transitions	490 ^{o}C			500 ^{o}C		
	$A_{rad}(s^{-1})$	β	τ_{rad}(ms)	$A_{rad}(s^{-1})$	β	τ_{rad}(ms)
$^4I_{13/2}\rightarrow{}^4I_{15/2}$	120.92	1	8.27	121.87	1	8.21
$^4I_{11/2}\rightarrow{}^4I_{15/2}$	109.03	0.81	7.43	111.95	0.80	7.15
$\rightarrow{}^4I_{13/2}$	26.34	0.19		28.65	0.20	
$^4I_{9/2}\rightarrow{}^4I_{15/2}$	103.80	0.77	7.42	106.52	0.76	7.13
$\rightarrow{}^4I_{13/2}$	32.19	0.23		33.71	0.24	
$^4F_{9/2}\rightarrow{}^4I_{15/2}$	1045.44	0.91	0.87	1062.76	0.91	0.86
$\rightarrow{}^4I_{13/2}$	55.56	0.05		56.20	0.05	
$\rightarrow{}^4I_{11/2}$	46.10	0.04		46.99	0.04	
$\rightarrow{}^4I_{9/2}$	2.39	0		2.36	0	
$^4S_{3/2}\rightarrow{}^4I_{15/2}$	787.92	0.67	0.85	809.75	0.67	0.83
$\rightarrow{}^4I_{13/2}$	324.19	0.27		333.17	0.27	
$\rightarrow{}^4I_{11/2}$	25.70	0.02		26.38	0.02	
$\rightarrow{}^4I_{9/2}$	42.86	0.04		43.82	0.04	

The spontaneous radiative transition probabilities (A_{rad}), branching ratios (β) and radiative lifetimes (τ_{rad}) of Er^{3+} in various samples are calculated by using the J-O intensity parameters and presented in Table S2. The A_{rad} for Er^{3+}: $^4I_{11/2} \rightarrow {}^4I_{13/2}$ transition increases from 22.06 s^{-1} to 28.65 s^{-1} with increasing heat-treatment temperature, which are comparable to those of ZBLAY (29.04 s^{-1}) and germanate (26.07 s^{-1}) glass.[4,5] Higher spontaneous radiative transition probability provides a better opportunity to achieve laser actions.

The emission cross section (σ_{em}) is calculated from the emission spectra by using the Fuchtbauer-Ladenburg equation:

$$\sigma_{em}(\lambda) = \frac{\lambda^5 A_{rad} I(\lambda)}{8\pi c n^2 \int \lambda I(\lambda) d\lambda} \tag{1}$$

The absorption cross section (σ_{abs}) can be calculated by McCumber equation:[6]

$$\sigma_{em}(\lambda) = \sigma_{abs}(\lambda)(Z_l/Z_u)\exp[(\varepsilon - h\nu)/KT] \tag{2}$$

where λ is the emission wavelength, A_{rad} is the spontaneous radiative transition probability of Er^{3+}: $^4I_{11/2} \rightarrow {}^4I_{13/2}$ transition, I(λ) is the 2.7 μm emission intensity, ∫I(λ)dλ is the integrated emission intensity, n is the refractive index, c is the light speed in vacuum, Z_l and Z_u are partition functions of the lower and upper manifolds, respectively, ε is the net free energy demanded to excite one electron of Er^{3+} from the $^4I_{13/2}$ to $^4I_{11/2}$ state, h is Planck's constant, K is the Boltzmann constant, and T is the temperature. By combining these two equations, the absorption and emission cross sections are calculated and shown in Figure S5a. The calculated peak absorption and emission cross sections at 2.7 μm are 0.57×10^{-20} cm^2 and 0.73×10^{-20} cm^2, respectively. The emission cross section of this GC sample is higher than those of tungsten-tellurite (0.61×10^{-20} cm^2), fluorophosphate (0.65×10^{-20} cm^2), and bismuth germanate (0.66×10^{-20} cm^2) glass, etc.[7-9]

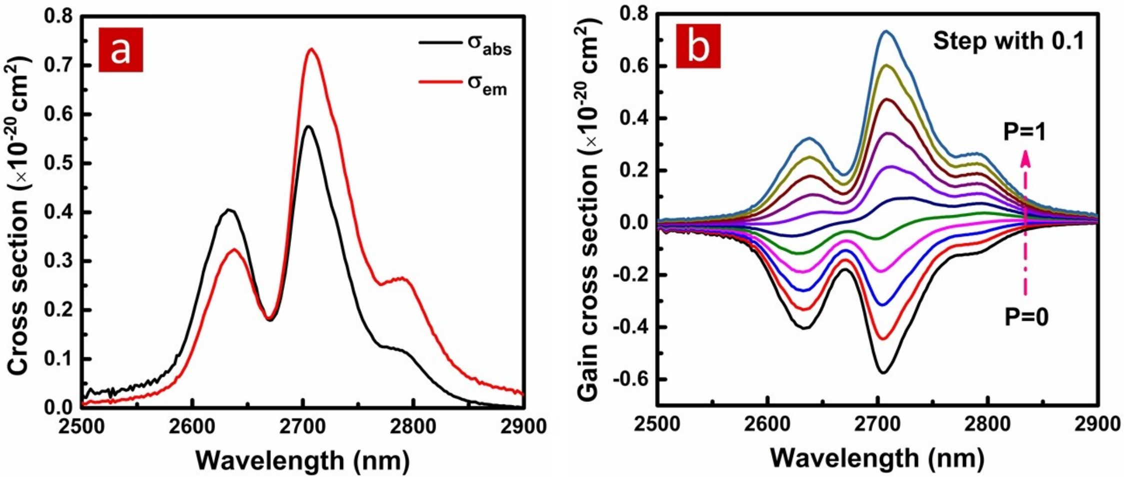

Figure S6. a) Absorption and emission cross sections, and b) gain cross sections at 2.7 μm in GC heat-treated at 500 °C for 5 h.

According to the absorption and emission cross sections, the gain cross section can be determined by

$$G(\lambda, P) = P\sigma_{em}(\lambda) - (1-P)\sigma_{abs}(\lambda) \tag{3}$$

where P is the population inversion corresponding to the concentration ratio of Er^{3+} between the $^4I_{11/2}$ level and the total Er^{3+} concentration. The gain cross section for various values of P ranging from 0 to 1 are displayed in Figure S5b. It can be observed that the positive gain appears when P is around 0.5, indicating that the pump threshold for achieving mid-infrared laser is relatively high.

Table S3. The parameters of Er^{3+}-doped GC fiber used in the calculation

Parameters	Value
λ_p	980 nm
λ_s	2.7 μm
τ	3.04 ms
σ_{ap}	0.21×10^{-20} cm^2
σ_{ep}	0.23×10^{-20} cm^2
σ_{as}	0.57×10^{-20} cm^2
σ_{es}	0.73×10^{-20} cm^2
A_c	5.5×10^{-6} cm^2
N	2.58×10^{20} cm^{-3}
α_p	5×10^{-5} cm^{-1}
α_s	3×10^{-5} cm^{-1}
Γ_p	0.85
Γ_s	0.78
L	10 m
R_1	0.98
R_2	0.04

References

1. X. X. Lin, F. F. Zhang, S. L. Pan, H. W. Yu, F. Y. Zhang, X. Y. Dong, S. J. Han, L. Y. Dong, C. Y. Bai and Z. Wang, J. Mater. Chem. C, 2014, **2**, 4257.
2. H. Assaaoudi, G. B. Shan, N. Dyck and G. P. Demopoulos, *CrystEngComm*, 2013, **15**, 4739.
3. H. Fares, W. Stambouli, H. Elhouichet, B. Gelloz and M. Ferid, *RSC Adv.*, 2016, **6**, 31136.
4. Y. Tian, R. R. Xu, L. L. Hu and J. J. Zhang, *Opt. Mater.*, 2011, **34**, 308.
5. T. Wei, F. Z. Chen, Y. Tian and S. Q. Xu, *J. Quant. Spectrosc. Ra.*, 2014, **133**, 663.
6. D. E. McCumber, *Phys. Rev.*, 1964, **136**, A954.
7. Y. Y. Guo, Y. Y. Ma, F. F. Huang, Y. P. Peng, L. Y. Zhang and J. J. Zhang, *Spectrochim. Acta Part A Mol. Biomol. Spectrosc.*, 2013, **111**, 150.
8. Y. Tian, R. R. Xu, L. Y. Zhang, L. L. Hu and J. J. Zhang, *Opt. Lett.*, 2011, **36**, 109.
9. G. Y. Zhao, Y. Tian, H. Y. Fan, J. J. Zhang and L. L. Hu, *Chin. Opt. Lett.*, 2012, **10**, 091601.